ADVANCED OPTICAL MATERIALS
www.advopticalmat.de

Optical Properties of Slot-Die Coated Hybrid Colloid/Cellulose-Nanofibril Thin Films

*Constantin Harder, Alexandros E. Alexakis, Yusuf Bulut, Shuxian Xiong, Benedikt Sochor, Guangjiu Pan, Huaying Zhong, Korneliya Goordeyeva, Manuel A. Reus, Volker Körstgens, Arno Jeromin, Thomas F. Keller, L. Daniel Söderberg, Eva Malmström, Peter Müller-Buschbaum, and Stephan V. Roth**

Correlating nanostructure and optical properties of thin hybrid films is the crucial ingredient for designing sustainable applications ranging from structural colors in anticounterfeiting to sensors. Here, the tailoring of the refractive index of hybrid cellulose nanofibril/water-dispersed colloidal ink thin films is presented. The authors apply scalable, layer-by-layer slot-die coating for preparing the cellulose nanofibril and hybrid thin films. Making use of the mobility of the polymer chains in the colloids upon annealing, the influence of the different colloid sizes and their glass transition temperature on the refractive index of the hybrid material is shown. The complex refractive indices of the thin films are characterized by spectroscopic ellipsometry and correlated to the different nanostructures of the thin films. The authors find that post-deposition annealing changes the colloidal nanostructure from particulate to agglomerates. Depending on the size of the colloids, imbibition of the colloids into the cellulose nanofibril template is observed. This scalable approach offers new avenues in structural color functional biomaterial hybrid layers.

1. Introduction

In nature, a fascinating example of structural color is the blue color in fauna which is achieved by hierarchical nanostructures.[1–3] The ordered arrangement of the colloids gives rise to the interference color. Here, one big advantage of structural colors based on colloids is their photostability which is advantageous compared to pigment-based color.[4]

Mimicking nature-inspired nanostructures, such non-iridescent structural colors find manifold applications.[5,6] For example, a one-pot synthesis allows for non-iridescent, freestanding multicolor films, inspired by mussel oxy-polymerization.[7] As the colloidal spacing directly affects the color,[8] ligands enable designed spacings and thus color tunability.[9] For sensors, switchable structural colors are achieved by tailored hydrophobicity and different pH values directly affecting the nanostructure.[10] Combining colloidal templating with thermoresponsive hydrogels, angle-independent, core-shell color sensors with inverse opal structure becomes feasible.[11] The color change is induced by changing the distance of the nanovoids.

Exploiting structural colors based on sustainable bio-derived materials show great potential. 3D disordered networks, such as

C. Harder, Y. Bulut, S. Xiong, B. Sochor, A. Jeromin, T. F. Keller, S. V. Roth
Deutsches Elektronen-Synchrotron DESY
Notkestr. 85, 22607 Hamburg, Germany
E-mail: stephan.roth@desy.de

C. Harder, Y. Bulut, S. Xiong, G. Pan, H. Zhong, M. A. Reus, V. Körstgens, P. Müller-Buschbaum
Chair for Functional Materials
Department of Physics
TUM School of Natural Sciences
James-Franck-Str. 1, 85748 Garching, Germany

The ORCID identification number(s) for the author(s) of this article can be found under https://doi.org/10.1002/adom.202203058

© 2023 The Authors. Advanced Optical Materials published by Wiley-VCH GmbH. This is an open access article under the terms of the Creative Commons Attribution License, which permits use, distribution and reproduction in any medium, provided the original work is properly cited.

DOI: 10.1002/adom.202203058

A. E. Alexakis, K. Goordeyeva, L. D. Söderberg, E. Malmström, S. V. Roth
Department of Fibre and Polymer Technology
KTH Royal Institute of Technology
Teknikringen 56-58, 10044 Stockholm, Sweden

A. E. Alexakis, L. D. Söderberg, E. Malmström
Wallenberg Wood Science Center (WWSC)
KTH Royal Institute of Technology
Teknikringen 56-58, Stockholm 10044, Sweden

A. Jeromin, T. F. Keller
Centre for X-ray and Nano Science CXNS
Deutsches Elektronen-Synchrotron (DESY)
22607 Hamburg, Germany

A. Jeromin, T. F. Keller
Department of Physics
University of Hamburg
Notkestraße 9-11, 22607 Hamburg, Germany

P. Müller-Buschbaum
Heinz Maier-Leibnitz-Zentrum (MLZ)
Technische Universität München
Lichtenbergstr. 1, 85748 Garching, Germany

fibrous materials, enhance light scattering and white light reflectance depending on phase percolation, angular correlation, and network valence.[12–14] Often, cellulose nanocrystals (CNC) are used for structural colors, for example, in dried films forming nematic hierarchical nanostructures.[15] Due to the evaporation-induced self-assembly, ordered structures occur, which are responsible for the structural colors.[16] When using cellulose nanocrystals' arrangements, one determining parameter of the structural color is the helical stacking[17] with a blue-shift of the reflected intensity due to a changing pitch and the expulsion of water during drying increasing the refractive index contrast. The structural color is directly affected by the size of the colloids and can be enhanced by the dielectric medium.[18] For isotropic, non-crystalline colloidal multilayers, the color is highly affected by the film thickness and colloidal size and independence from the angle of observation.[19] Concerning one-pot synthesis, CNCs are also used as a template to synthesize silver-core:gold-shell nanoparticles.[20] Furthermore, silk can be used to create optically active materials, for example, bioactive[21] and even as feedback materials in lasers.[22]

The lightweight flexible materials are wood-based cellulose nanofibrils (CNF).[23] CNF with radii of around 2.5 nm and lengths of around 600 nm with an applied surface charge[24] are recently used as novel templates in organic electronics.[25] Blending CNF with nanoparticles has two advantages. To start with inorganic nanoparticles, a composite of CdS quantum dots (QDs) and CNFs allows for adjusting fluorescent colors by tuning the QD size.[26] On the other hand, layer-by-layer-deposited silver nanoparticle-CNF bilayers show a changing localized surface plasmon resonance due to the combined action of reduced coffee ring effect and CNFs as a dielectric medium,[27] which is useful in sensor applications.[28,29] Furthermore, by using nanoparticle precursor and thermal treatment, the plasmonic properties of the final silver nanoparticles can be tuned due to the activity of CNFs.[30] Light-matter interactions on the molecular level like plasmon resonances allow for stimulating movements on soft and bio-interfaces, thus even enabling light-driven actuators.[31,32]

In order to improve the mechanical properties of pure biomaterials, cellulose-based materials can be blended with inorganic polymer colloids.[33–35] Inorganic nanoparticles are able to directly cross-link the CNFs via radical polymerization of stearyl acrylate.[36] The introduction of ionic liquids similarly improves mechanical and optical properties after hot-pressing.[37]

The above-mentioned examples show that understanding the optical properties of bio-based and colloidal functional layers is essential for flexible optoelectronics applications.

For determining optical constants of thin films, namely refractive index and attenuation coefficient, ellipsometry, and white light interferometry are the methods of choice.[38–41]

X-ray scattering methods are ideally used to determine porosity and colloidal arrangement. In amorphous colloidal crystals, transmission small-angle X-ray scattering (SAXS) allows for determining the spacing of the colloids.[19,42] For thin films, grazing incidence X-ray and neutron scattering (GISAXS/GISANS) allow for quantifying the network structure[43,44] and chiral properties.[45] Here, the X-ray or neutron beam impinges under a shallow angle onto the sample surface and is scattered diffusively. This geometry allows for analyzing the complex, layered thin film nanostructure in both vertical and horizontal (with respect to the sample surface) directions[46–48] and correlating it with the films' optical properties.[49,50]

In order to derive the nanostructure-function relationship, the combination of GISAXS and ellipsometry has proven its use.[51] This combination allows to in situ derive optical and nanostructural maps of colloidal arrangements during evaporation-induced self-assembly.[52] Thermal treatment of spin-coated polystyrene colloidal layers enables tuning of the refractive index by tuning the porosity of the thin film.[53] When crossing the glass transition temperature during heating up, the polymer chains become mobile, the spherical shape of the colloids is lost, and the layer density increases. As a result, this increases the refractive index. In colloidal mixtures of gold and polystyrene nanospheres, a phase separation between the small metallic and large polymeric nanoparticles is observed during drying.[50] Selective wetting of physical vapor-deposited gold nanoparticles in imprinted polymer films can be explored at curves surfaces.[54] Furthermore, GISAXS allows for determining directional, hierarchical structures[55] and spectroscopic ellipsometry for correlating this complex nanostructure to its optical response.[49] Extending to molecular arrangements in gratings, the combination with grazing incidence wide-angle X-ray scattering (GIWAXS) allows for correlating optical response, molecular arrangement, and grating morphology.[45,56]

In terms of fabricating hybrid thin films, scalable layer-by-layer coating from the liquid phase is especially useful for colloidal and cellulose-based dispersions. To start with, ink-jet printing allows the facile deposition of multi-color functional layers.[57] For conformal, 3D coatings, spray deposition is a versatile and scalable route. It relies on the atomization of colloidal dispersions and allows color mixing by multilayer coatings.[58,59] Slot-die coating is readily applied in photovoltaics and flexible electronics[60,61] and for facilitating QD multilayer devices.[62] It allows for installing large-area devices and allows for more effective use of the supplied material, compared, for example, to spin coating.

In this work, we correlate the nanostructure and optical properties of novel slot-die coated hybrid core-shell colloid-CNF thin films. Here, CNF acts as a sustainable, nanoporous template; depending on the colloid size, imbibition of the colloids occurs and leads to intermixing layers. Secondly, we correlate the nanostructural changes of the colloids in the hybrid films upon thermal post-treatment with the colloids' stability and the changes in optical properties, both refractive index and absorption. We use two different deposition techniques for fabricating the CNF films, namely, spray deposition[44,48] and slot-die coating. During deposition, CNF forms a film with a nanoporous network. This network is transparent to visible light and together with the thickness the color can be changed.[63,64] The films deposited on silicon wafers have a thickness of ≈140 nm, which corresponds to a blue surface color. As colloidal ink, two different types of core-shell colloids were used. The first type consists of a core of poly(sobrerol methacrylate) (PSobMA) with different sizes, which we denote via subscriptS and L (radius ≈20/≈40 nm). The core of the second type is made from the block co-polymerpoly(sobrerol methacrylate-block-butyl methacrylate)(P(SobMA-co-BMA)) to tune the glass transition temperature and thus processability. The shell of the small colloids consists of 2-(dimethyl-amino)ethyl methacrylate

© 2023 The Authors. Advanced Optical Materials published by Wiley-VCH GmbH

Table 1. Characteristics of the used colloids.

	$PSobMA_S$	$PSobMA_L$	$P(SobMA\text{-}co\text{-}BMA)_S$	$P(SobMA\text{-}co\text{-}BMA)_L$
Glass transition temperature T_g [°C]	119 ± 7	123 ± 2	89 ± 3	74 ± 2
Radius [nm]	22 ± 9	39 ± 12	29 ± 6	44 ± 14
PDI	0.08 ± 0.01	0.09 ± 0.01	0.15 ± 0.02	0.17 ± 0.06

(PDMAEMA) and of the surfactant cetyltrimethylammonium chloride (CTAC) for the large ones. The colloids' names, sizes, and glass transition temperatures are summarized in **Table 1**. The interaction between colloids and CNF is due to electrostatic interaction: The colloids show a positive surface charge, while CNF has a negative surface charge due to TEMPO mediated oxidation.

To characterize the morphology of the spray-coated and slot-die coated CNF (negative surface charge of 1000 µmol g^{-1}, similar to those used for spinning fibers[24]) samples, GISAXS, scanning electron microscopy (SEM), atomic force microscopy (AFM), and spectroscopical ellipsometry (SE) was used. In particular, the focus was on the optical constants, the refractive index and extinctioncoefficient evaluated via spectroscopic ellipsometry. The slot-die-coated CNF template shows a higher refractive index and denser network owing to the deposition conditions. To deposit the CNF layer, multiple slot-printing iterations were performed. In contrast to spraying, no air flow as induced by the spray deposition is occurring, and the drying time is increased. Slot-die coating applies a dispersion film, leading to a smooth and structureless air-solvent interface, while spray deposition applies atomized droplets, which might induce coffee-ring effects. With the substrate temperature being the same in both deposition routes, both effects lead to a denser network in case of slot-die coating. In a second deposition step, a colloidal layer of core-shell colloids of two different sizes and glass transition temperatures (T_g) is applied via slot-die coating. This makes a total of four hybrid materials to be investigated. Both SE and GISAXS indicate partial imbibition of the colloids in the porous CNF template for the small colloids, as monitored by a higher refractive index at the same deposition parameter of the slot-die coating. After annealing above T_g, the refractive index of the hybrid structure with the larger colloids increases above that of the small colloid layer, indicating a higher reduction imbibition of the larger colloids. Additional atomic force microscopy (AFM) and field-emission scanning electron microscopy (FE-SEM) corroborate the results. Our results pave the route for sustainable hybrid colloid-cellulose thin films for structural color devices, for example, packaging sensors, anticounterfeiting, and templates for photovoltaics.[65]

2. Results

Figure 1 shows the fabrication of the hybrid CNF-colloid thin films. First, the CNF layer is slot-die coated, (Figure 1a). The CNF layer serves as a hydrophilic, porous template for the subsequent deposition of the colloidal ink.

After full drying of the template, the four different PSobMA-based colloidal dispersions $PSobMA_S$, $PSobMA_L$, $P(SobMA\text{-}co\text{-}BMA)_S$, $P(SobMA\text{-}co\text{-}BMA)_L$are slot-die coated on the CNF template using the same printing device and at room temperature

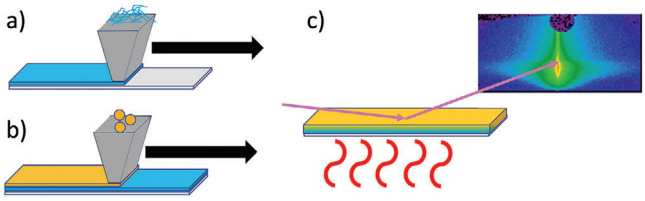

Figure 1. Scheme of the slot-die coated hybrid thin-film preparation. a) First, the cellulose nanofibril film is slot-die coated. b) Subsequently, the colloids are slot-die coated. c) Finally, annealing above the T_g is performed. The change of the nanostructure of the deposited colloids is monitored during annealing using grazing incidence small-angle X-ray scattering (GISAXS).

(Figure 1b). After applying the colloids on the CNF layer the hybrid systems are annealed (Figure 1c). The optical appearance is blueish for the CNFtemplate and orange after colloid deposition on the colloid domains, see Figures S1 and S2, Supporting Information. The details of the slot-die coating are given in the experimental section.

This approach allows for a layer-by-layer deposition of the different colloids. The subsequent annealing step allows for further tuning of the nanostructure and optical properties. The nanostructural change of the colloids is then monitored by GISAXS and correlated to the change in optical properties as characterized by the refractive index and extinction coefficient. The experimental details including materials and methods are presentedin the Experimental Section below.

In **Figure 2**a the refractive index of the slot-die-coated CNF template is visible compared to the well-known spray-deposited template. Spray deposition has been recently used for preparing nanoporous templates for organic electronics.[27,30] Spray-deposited layers thus serve as reference material. As both the deposition method and drying influence the nanostructure of hybrid materials,[48,66] changes in optical properties are expected. For example, a comparison between spray-deposited and spin-casted active layers for solar cells, reveals that spray-coated films have a larger surface roughness.[67] The spectroscopic ellipsometry (SE) results yield a larger refractive index at the same film thickness for the slot-die-coated film. The layer thickness as determined by SE is 140 ±1 nm for sprayed and 139.5 ± 0.5 nm for the slot-die coated film. Since both CNF films are of the same thickness and the refractive index of the printed CNF film is higher, we conclude that the slot-die coated film has a higher optical density. The calculated thickness of the slot-die-coated CNF layer agrees with the thickness measurement of Dektak thickness measurements of 145 ± 2 nm (Figure S3, Supporting Information). The wavelength dependence of the extinction coefficient is shown in Figure 2b. The slot-die-coated CNF layer shows a higher absorption loss in the visible, blue regime compared to

© 2023 The Authors. Advanced Optical Materials published by Wiley-VCH GmbH

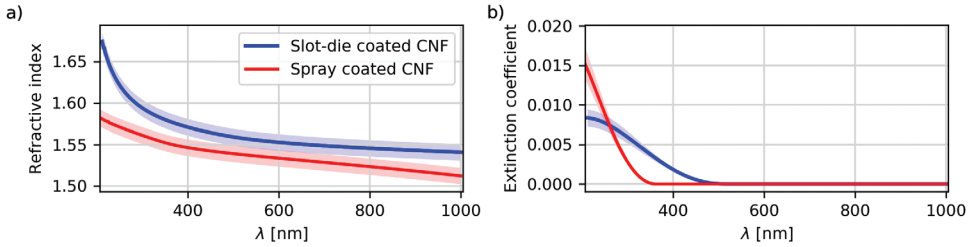

Figure 2. Spectroscopic ellipsometry (SE) results for sprayed and printed CNF films: a) Refractive index, b) Extinction coefficient.

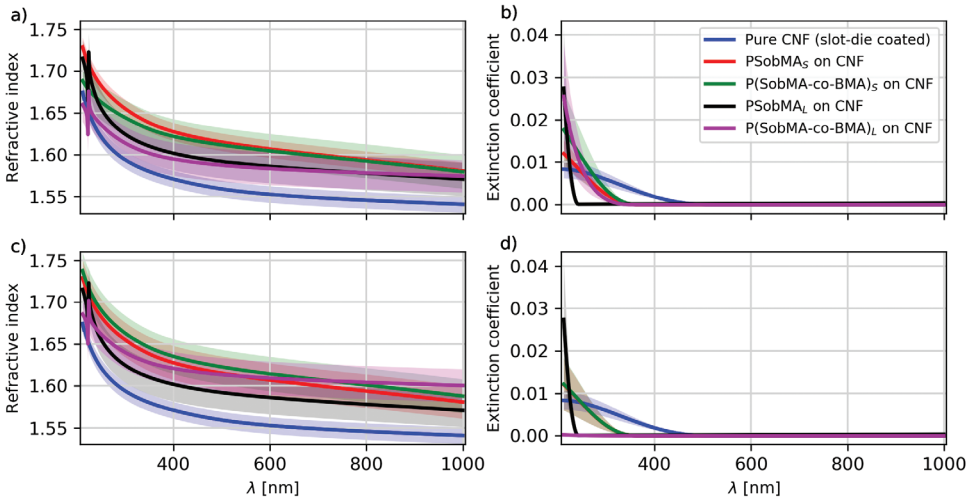

Figure 3. Temperature dependence of the a,c) refractive index and b,d) extinction coefficient of the uppermost layer for a,b) room temperature; c,d) T = 140 °C. For comparison, the results of the refractive index and extinction coefficient for the pure slot-die-coated CNF layer are included.

the spray-deposited layer. This might be due to the more compact CNF layer. The correlated roughness occurs due to the printing conditions. The steady flow of dispersion is balanced by the evaporation of the water and thus leads to a "smooth" deposition of the CNF allowing them to follow the substrate roughness. Spraying uses atomization prior to the deposition of droplets and thus makes correlated roughness more difficult to achieve.

Figure 3 shows the results for the refractive index and extinction coefficient of the uppermost layer after the deposition of the colloids before and after annealing. Two differently sized colloids were chosen. In addition, the glass transition temperature T_g was tuned by the materials used, see Table 1. From our previous studies of spray-deposited CNF films and the SE measurements, the pore sizes of the slot-die-coated CNF layer are around 50 nm.[44] Hence, small colloids with a radius of around 20 nm are expected to show already imbibition during slot-die coating, while the larger colloids (radius of ≈40 nm) are unlikely to penetrate into the CNF layer. In detail, pure CNF shows the lowest refractive index, see Figure 3a. For large colloid printing, PSobMA$_L$/CNF and P(SobMA-co-BMA)$_L$/CNF show quite similar refractive indexes, both above that of CNF. Below $\lambda_{vis} \leq 550$ nm, PSobMA$_L$ shows a higher refractive index than P(SobMA-co-BMA). For PSobMA$_S$/CNF and P(SobMA-co-BMA)$_S$/CNF, the trend is the same; however, when depositing small colloids, this hybrid material shows for both PSobMA$_S$ and P(SobMA-co-BMA)$_S$ the highest refractive index. The annealing induces chain mobility and thus coalescence and deformation of the colloids. After annealing (Figure 3c), there is only a small change in the refractive index of the PSobMA$_L$/CNF hybrid layer. For P(SobMA-co-BMA)$_L$/CNF, the refractive index approaches the refractive index of PSobMA$_S$/CNF and P(SobMA-co-BMA)$_S$/CNF. This is related to the difference in glass transition temperature. **Figure 4** shows the refractive index of the hybrid materials as a function of depth before and after annealing. Interestingly, PSobMA$_S$/CNF and PSobMA$_L$/CNF show no change in thickness, while P(SobMA-co-BMA)$_S$/CNF and P(SobMA-co-BMA)$_L$/CNF show a decrease. At the same time, their refractive index increases. The colloidal layer is more compact after the annealing in case the lower T_g colloids (P(SobMA-co-BMA)$_S$/CNF, P(SobMA-co-BMA)$_L$/CNF).

The extinction coefficient shows similar behavior for PSobMA$_S$/CNF and P(SobMA-co-BMA)$_S$/CNF, and P(SobMA-co-BMA)$_L$/CNF (Figure 3b). After annealing (Figure 3d), we observe strong changes only for P(SobMA-co-BMA)$_S$/CNF and P(SobMA-co-BMA)$_L$/CNF. P(SobMA-co-BMA)$_S$/CNF and PSobMA$_S$/CNF show nearly similar extinction coefficients.

For extracting the optical constants, we applied the following model, see **Figure 5**a. The model consists of a maximum of four layers. The substrate is pure silicon with a 2 nm thick layer of SiO_2. The printed CNF layer is a modeled layer with a thickness between 100 and 150 nm. To model the refractive index and the extinction coefficient of the CNF template, a semi-absorbing generalized oscillator layer was used (Table S1, Supporting Informa-

© 2023 The Authors. Advanced Optical Materials published by Wiley-VCH GmbH

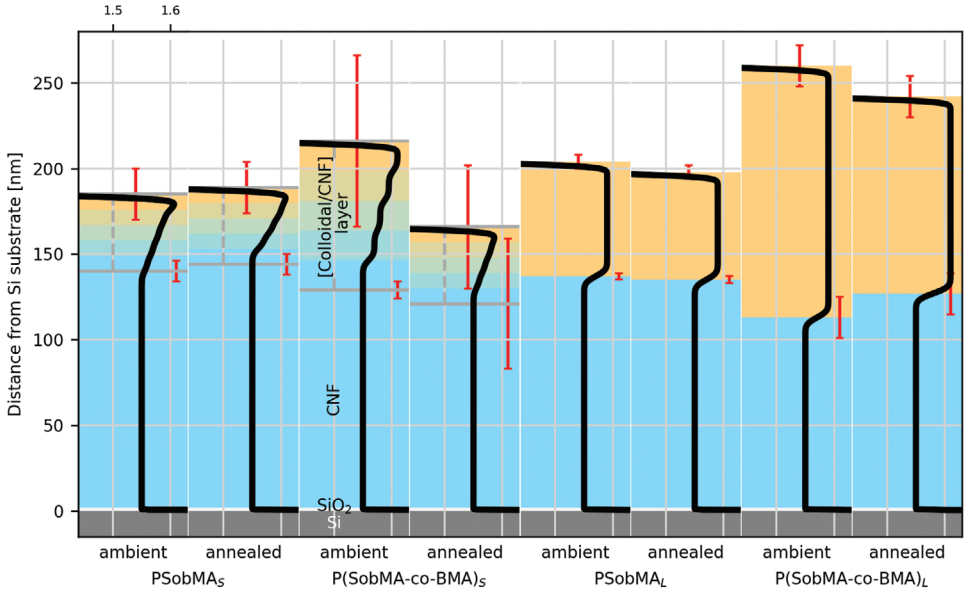

Figure 4. Depth dependence of the refractive index for the slot-die coated hybrid films. The depth dependence refractive index of the colloids with the high T_g (PSobMA) do not change. For the P(SobMA-co-BMA) colloids, the layer thickness is reduced and the refractive index is increased. This shows that the P(SobMA-co-BMA)$_L$ is more compact on the CNF.

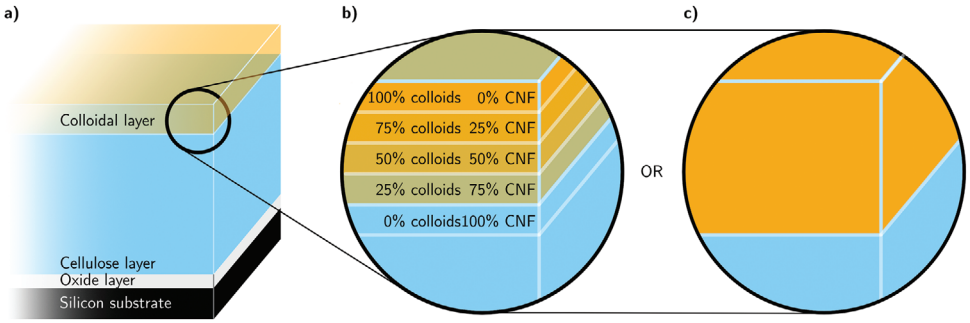

Figure 5. Sketch of the different layers to model the optical properties of a) the hybrid colloidal/CNF layer system. b) The slice stack for the small colloid/CNF hybrid thin film, and c) the homogenous layer for the large colloid/CNF hybrid thin film.

tion). This generalized oscillator layer is based on three Cody–Lorentz functions to model the imaginary permittivity ϵ_2. On the CNF layer, the coated colloidal layer was modeled (Table S2, Supporting Information).

Due to the size of the smaller colloids being comparable to the voids in the CNF template, thus allowing for imbibition, PSobMA$_S$ and P(SobMA-co-BMA)$_S$ are modeled as a graded layer (Figure 5b). This graded layer is subdivided into five slices with a thickness of 45 ± 15 nm in case of PSobMA$_S$ and 87 ± 50 nm in case of P(SobMA-co-BMA)$_S$, see **Table 2.** The thickness of the CNF layer was derived as 138 ± 5.5 nm (PSobMA$_S$) and 127 ± 5 nm (P(SobMA-co-BMA)$_S$). The total layer thicknesses (corresponding to the sum of the CNF layer and colloidal layer thicknesses) are retrieved as 183 ± 21 and 214 ± 55 nm, respectively, being within the error estimates roughly the same in both cases. In detail, the lowest slice of the graded layer is considered to be CNF. Each slice is modeled as a homogenous layer including the top layer. The top slice is considered to be a pure colloidal layer. The three intermediate slices establish a gradient from the refractive index of the colloids to the refractive index of CNF. The graded layer manifests itself as a gradual change in the refractive index.

The optical properties of the hybrid materials PSobMA$_L$/CNF and P(SobMA-co-BMA)$_L$/CNF are modeled by a homogenous CNF layer and colloidal layer without any mixing layer, see Figure 5c. The corresponding CNF layer and colloidal layer thicknesses are derived as 135 ± 2 and 67 ± 4 nm for PSobMA$_L$/CNF as well as 111 ± 12 and 147 ± 12 nm for P(SobMA-co-BMA)$_L$/CNF. The colloid sizes are 78 and 88 nm respectively. The larger thickness might indicate stronger agglomerations for P(SobMA-co-BMA)$_L$ colloids. The total layer thicknesses of the CNF and colloidal layers are 202 ± 6 and 258 ± 24 nm, respectively.

The full wavelength dependence is shown in Supporting Information. The resultsindicatethe imbibition ofsmall colloids into the nanoporous CNF layer already during deposition. After

© 2023 The Authors. Advanced Optical Materials published by Wiley-VCH GmbH

Table 2. Results for layer thicknesses from fitting the spectroscopic ellipsometry data. "SUM" denotes the total thickness.

	Annealed	CNF layer thickness [nm]	Colloidal CNF layer thickness [nm]	SUM[nm]
$PSobMA_S$	–	138 ± 6	45 ± 15	183 ± 21
$PSobMA_L$	–	135 ± 2	67 ± 4	202 ± 6
$P(SobMA\text{-}BMA)_S$	–	127 ± 5	87 ± 50	214 ± 55
$P(SobMA\text{-}BMA)_L$	–	111 ± 12	147 ± 12	258 ± 24
$PSobMA_S$	Yes	142 ± 6	45 ± 15	187 ± 21
$PSobMA_L$	Yes	133 ± 2	63 ± 4	196 ± 6
$P(SobMA\text{-}co\text{-}BMA)_S$	Yes	119 ± 38	45 ± 36	164 ± 74
$P(SobMA\text{-}co\text{-}BMA)_L$	Yes	125 ± 12	115 ± 12	240 ± 24

full drying and at room temperatures the refractive indices of $PSobMA_S$ and $P(SobMA\text{-}co\text{-}BMA)_S$ are higher than for $PSobMA_L$ and $P(SobMA\text{-}co\text{-}BMA)_L$, as part of the CNF layer being filled with small colloids due to imbibition as a result of the similar sizes of nanopores and small colloids.[44]

After annealing, $PSobMA_S$/CNF shows only minor changes in the CNF and graded layer thicknesses (142 ± 6, and 45 ± 15 nm). The errors are calculated during the fitting (see Table S2, Supporting Information). For $P(SobMA\text{-}co\text{-}BMA)_S$/CNF, the CNF layer shows within error limits a similar thickness of 119 ± 38 nm, as well as for the colloid layer thickness of 45 ± 36 nm due to the large error in both cases. The same holds for the total layer thicknesses of 187 ± 21 and 164 ± 74 nm, respectively. The modeling included the same graded layer as mentioned above.

For the large colloids, the modeling was also unchanged after annealing compared to the as-deposited case. $PSobMA_L$/CNF shows CNF thickness, colloidal layer thickness, and total thickness of 133 ± 2, 63 ± 4, and 196 ± 6 nm respectively. In case of $P(SobMA\text{-}co\text{-}BMA)_L$/CNF, the corresponding thicknesses are evaluated as 125 ± 12, 115 ± 12, and 240 ± 24 nm. Here, the colloidal layer seems to be slightly thinner after annealing, which we attribute to the lower T_g of P(SobMA-co-BMA). To summarize, depending on the sizes of the colloids, the SE data reveal the imbibition of the colloids. After annealing, the multilayer structures are rather unchanged except for $P(SobMA\text{-}co\text{-}BMA)_L$/CNF. In the latter case, the smaller colloidal layer thickness might be interpreted as a small, partial imbibition of the mobile polymer chains into the CNF layer, as the total layer thickness is similar.

In order to correlate the findings from SE with the nanoscale structure of the hybrid films, we characterized the different thin films by GISAXS. **Figure 6**a–c shows the 2D GISAXS pattern of the spray-deposited and the slot-die coated CNF layer with the X-ray beam impinging in the printing direction and perpendicular to it. The GISAXS pattern of the spray-deposited thin film differs strongly from that of the slot-die coated. The intensity evolution $I(q_z)$ (so-called vertical cut, see Figures S4 and S5, Supporting Information) shows strong fringes in case of the slot-die coated ones. This so-called resonant-diffuse scattering is indicative of a well-reproduced roughness of the underlying substrate.[68,69] We conclude that slot-die coating is much more favorable than spray-deposition in terms of correlated roughness. Secondly, the intensity evolution $I(q_y)$ probing structures parallel to the sample surface, that is, distances and radii of nanostructures, extends much further to lower q_y. This is again indicative of a much better roughness correlation in slot-die-coated films. In contrast to spray deposition, the slot-die coating has a preferred deposition direction due to the printhead movement. Figure 6b,c) show the 2D GISAXS pattern of the slot-die coated CNF layer with the X-ray beam impinging in the printing direction and perpendicular to it. The corresponding horizontal line cuts are shown in Figure 6d. We note that the intensity for the parallel geometry (green curve in Figure 6d) is slightly above that of the perpendicular geometry (blue curve in Figure 6d) above $q_y \cong 0.03\ nm^{-1}$. Qualitatively, this might be due to a small alignment of the CNF in the printing direction due to shear.[70] The FE-SEM image (Figure 6e) shows a more disordered arrangement, implying the potential sub-surface ordering of the CNFs. However, the local AFM or SEM images show a more disordered nanostructure. In our case, a potential small alignment is not relevant and will not be considered further in this work. The detailed analysis of the GISAXS data yields CNF structures with radii of R_I = 7.5 ± 0.5 nm, R_{II} = 35 ± 5 nm, and R_{III} = 160 ± 10 nm. Following our previous work,[27,44,48] these structures correspond to bundles of CNF, voids, and larger-scale agglomerations, respectively. All extracted fit parameters are shown in Table S3, Supporting Information.

Now, we observe the imbibition properties of the novel slot-die-coated CNF layers, to study their usability as templates for colloid/CNF hybrid materials, and further research will focus on them.

After slot-die coating at room temperature, we observe structures of R($PSobMA_S$/CNF) = 19 ± 1 nm, R($PSobMA_L$/CNF) = 37 ± 3 nm, R($P(SobMA\text{-}co\text{-}BMA)_S$/CNF) = 18 ± 1 nm, and R($P(SobMA\text{-}co\text{-}BMA)_L$/CNF) = 36 ± 4 nm. These radii correspond well with the reported ones.[33] With GISAXS we followed the annealing process in situ. At T = 70 °C, no significant change in colloid structure is observed. At T = 100 °C, R($P(SobMA\text{-}co\text{-}BMA)_S$/CNF) increases to = 24 ± 2 nm, that is, a flattening of these colloids. R($P(SobMA\text{-}co\text{-}BMA)_L$/CNF) does still not change significantly due to the lower surface-to-volume ratio of the larger colloids. At T = 140 °C, R($PSobMA_L$/CNF) = 35 ± 3 nm remains still unchanged, while R($PSobMA_S$/CNF) = 20 ± 1 nm increased slightly. However, the core-shell copolymer colloids' radius increased drastically to R($P(SobMA\text{-}co\text{-}BMA)_S$/CNF) = 45 ± 3 nm and R($P(SobMA\text{-}co\text{-}BMA)_L$/CNF) = 67 ± 10 nm, showing the complete loss of structural integrity of the colloids.[71,72] The CNF structures remain unchanged. The corresponding temperature-dependent 2D GISAXS pattern, horizontal cuts, and fits are shown in Figures S5–S9, Supporting Information. **Figure 7** shows the temperature evolution of the different structures, extracted from the horizontal cuts. Exemplary horizontal cuts are shown in Figure 6f for $P(SobMA\text{-}co\text{-}BMA)_S$/CNF. For the PSobMA colloids with a $T_g \approx 120$ °C, only annealing at T = 140 °C was performed, as structural changes are not expected for 70 and 100 °C.[72] **Table 3** details the volume fraction of CNF bundles, voids, large agglomerations, and colloids for the hybrid materials before and after annealing. The volume percentage of the void structure remains constant after colloid deposition. After annealing, the colloid volume fraction decreases due to the establishment of larger-scale structures, partially observed in FE-SEM, see **Figure 8**. These larger structures lead to an increase of

© 2023 The Authors. Advanced Optical Materials published by Wiley-VCH GmbH

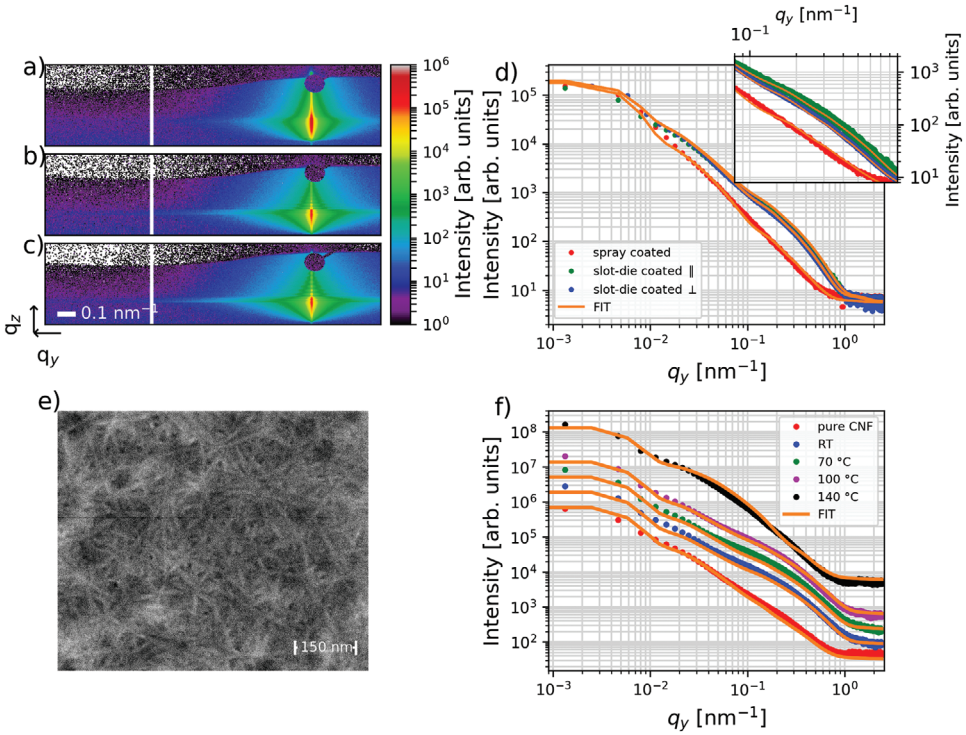

Figure 6. 2D GISAXS data of a) spray-deposited CNF film, b) slot-die-coated CNF film perpendicular to printing direction, and c) slot-die-coated CNF film parallel to the printing direction. d) The horizontal line cuts of the slot-die-coated CNF layer. ∥ denotes the X-ray beam direction parallel to the slot-die coating direction, ⊥ the X-ray beam direction perpendicular to the slot-die coating direction. The inset shows a zoom-in between 0.08 and 0.8 nm^{-1}. e) Scanning electron microscopy image of the slot-die coated CNF layer. f) Horizontal line cuts for the in situ annealing of P(SobMA-co-BMA)$_S$/CNF. The solid lines are fitted to the experimental data.

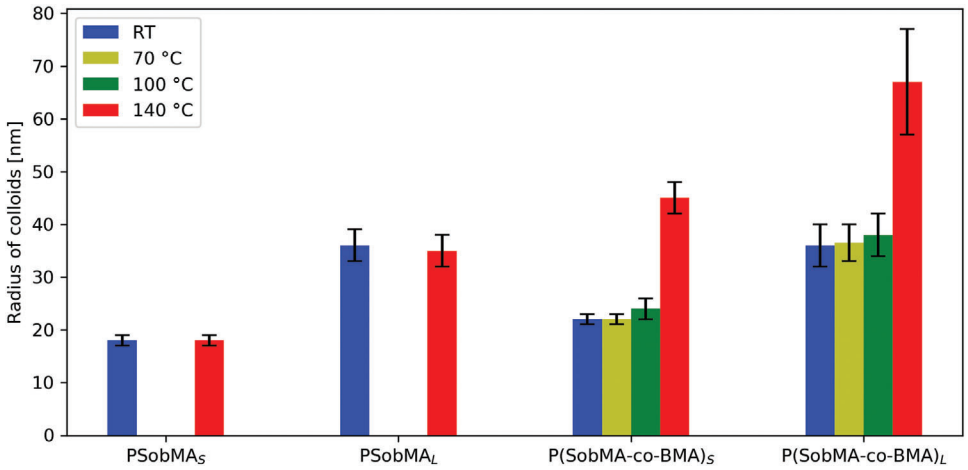

Figure 7. Evolution of radii of the nanostructures in the CNF layers and hybrid films as a function of annealing temperature.

the intensity in Figure 5e) around 0.01 nm^{-1} and overlap with the large agglomerations of CNF.

FE-SEM and AFM images for P(SobMA-co-BMA)$_L$/CNF are presented in Figure 8. The images of the other three hybrid materials are presented in Figures S10–S12, Supporting Information.

In detail, Figure 8a1–a3 shows the surface topography of the hybrid thin film after slot-die coating prior to annealing. The spherical colloids are visible. In the phase image Figure 8a3), the CNFs are visible. After annealing at T = 140 °C (Figure 8b1–b3), the presence of larger agglomerations on the surface is observed. The underlying CNF template is well visible, showing no structural change, even after annealing. The larger agglomerations lead to the above-mentioned increase of the scattered intensity in the GISAXS pattern round $q_y \sim 0.01$ nm^{-1}, see Figure 6f and Figure S7, Supporting Information. AFM images (Figures S10–S12, Supporting Information) corroborate the partial loss

© 2023 The Authors. Advanced Optical Materials published by Wiley-VCH GmbH

Table 3. Volume fraction of the nanostructures in %.

Structure	CNF bundles	Voids	Agglomerations	Colloids
CNF	85.5 ± 1.5	11.6 ± 1.7	3 ± 0.2	–
$PSobMA_S$ on CNF	82 ± 1	11.1 ± 1.2	2.9 ± 0.2	3.7 ± 0.2
$PSobMA_S$ on CNF, annealed	83 ± 1	11.2 ± 0.9	2.8 ± 0.3	2.9 ± 0.3
$P(SobMA\text{-}co\text{-}BMA)_S$ on CNF	82 ± 1	11.1 ± 1.4	1.9 ± 0.5	4.9 ± 0.3
$P(SobMA\text{-}co\text{-}BMA)_S$ on CNF, annealed	83 ± 1.3	11.2 ± 1.4	1.9 ± 0.5	3.8 ± 0.3
$PSobMA_L$ on CNF	84 ± 1.5	11.4 ± 1.2	2.9 ± 0.4	1.7 ± 0.4
$PSobMA_L$ on CNF, annealed	84 ± 1.2	11.3 ± 1.3	2.9 ± 0.4	1.9 ± 0.3
$P(SobMA\text{-}co\text{-}BMA)_L$ on CNF	84 ± 1.4	11.3 ± 0.9	2.8 ± 0.3	1.9 ± 0.4
$P(SobMA\text{-}co\text{-}BMA)_L$ on CNF, annealed	84 ± 1.1	11.4 ± 1.0	2.9 ± 0.3	1.5 ± 0.5

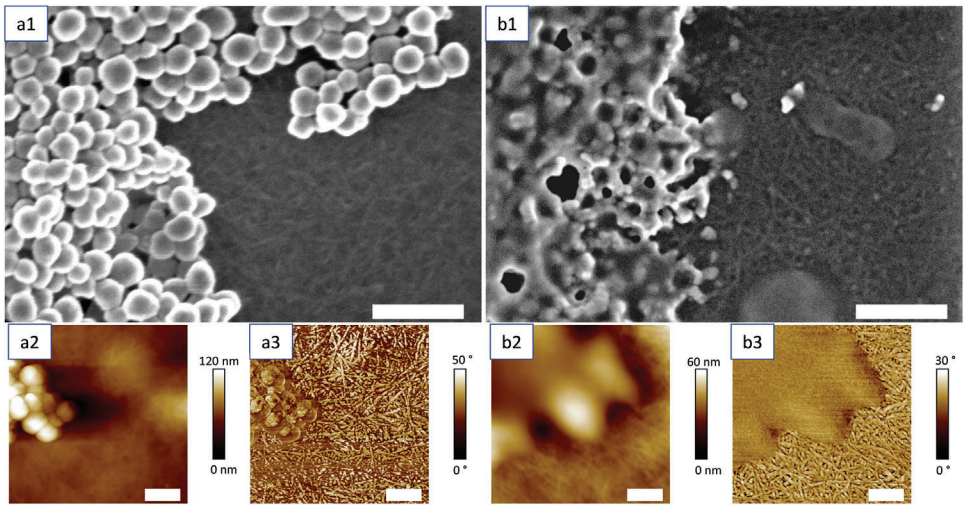

Figure 8. Secondary electron images (FE-SEM) of $P(SobMA\text{-}co\text{-}BMA)_L$/CNF after a1) slot-die coating and b1) after annealing. The scale bar corresponds to 300 nm. a2,3) Corresponding height and phase AFM images after slot-die coating, and b2,3) after annealing.

of structural integrity of the colloids. In detail, the AFM images reveal the structural integrity of all colloids at $T = 25$ °C. Upon annealing, the structural integrity is lost for $P(SobMA\text{-}co\text{-}BMA)_S$ and $P(SobMA\text{-}coBMA)_L$. Yet, for $PSobMA_L$ and $PSobMA_S$. some colloids are still visible at T = 140 °C. The GISAXS data (Figure S13 and Table S4, Supporting Information) reveal no influence on the correlated roughness after annealing.

3. Discussion

Creating structural color based on porous templates and colloids necessitates the fabrication of hybrid thin films. Slot-die coating presents a scalable and robust route for designing such hybrid materials as thin films. The imbibition properties are governed by the surface properties of the porous template.[73] This includes surface charge and hydrophilicity as well as the pore size. Additionally, the surface roughness influences the wetting properties for aqueous dispersions. Focusing on CNF as sustainable templates we explore the replacement of synthetic materials. We use them to fabricate a porous biomaterial-based template: CNFs offer the possibility of tuning their surface charge by functionalization and thus tuning the imbibition properties.[44,74] The CNF used here has a negative surface charge of 1000 µmol g^{-1}, known to minimize the water contact angle and thus favor the imbibition properties of water-based dispersions.[27,44] Such CNF templates show a nanopore size of several 10 nm. This makes them ideal templates for functional hybrid by applying colloids. The colloids as applied here have a positive surface charge.[33] Thus, the structure formation of the applied colloids is governed by electrostatic interactions and interaction with the CNF template.[75] In addition, the CNF chosen show minimal contact angle,[44] thus favoring imbibition of water-based dispersions. We expect that if the template material has the same topology (i.e., morphology and physicochemical properties) as the CNF thin films, we expect similar arrangement and similar optical properties. The morphology of the CNF thin films also depends on the coating technique, which is visible in the GISAXS data, refractive index, and extinction coefficient.

Structural colors are tunable by colloidal size and arrangement.[18] The colloidal arrangement is tailorable by the deposition method as well as by the use of a designed shell and post-deposition treatment. Using advanced core-shell colloids with a tunable glass transition temperature of around 100 °C allows for inducing nanostructural changes without inducing

© 2023 The Authors. Advanced Optical Materials published by Wiley-VCH GmbH

changes in the CNF template. This can be used in advanced autonomous manipulation-free temperature sensors.[76]

4. Conclusion

We investigated the nanostructure-optical properties relationship of core-shell colloid-CNF hybrid materials. To start with, we compared two relevant deposition methods (spray- versus slot-die coating of the CNFs). The surface roughness of the novel slot-die-coated CNF template is small compared to the spray-coated cellulose films. Furthermore, the slot-die coated CNF shows correlated roughness. Slot-die-coated CNFs have a higher refractive index than spray-coated CNFs. This implies that slot-die-coated CNF films have a higher density than spray-coated films. These slot-die-coated films serve as model systems that allow the application of core-shell colloids: This approach allows for understanding fundamental interactions of the different components, for deriving processing routes and for quantifying the influence of nanostructure on the optical properties.[77] In our case, we used two core-shell colloid systems with different sizes and different T_g. The different colloid size allows for selective imbibition during slot-die coating. The different T_g allowed for tuning the colloid layer structure. Additionally, the printing of the colloids on CNF leads to a strong color change from blue to orange of the film, which is a manifestation of an interference color. The optical properties are quantified by spectroscopic ellipsometry. With the CNF template having the lowest refractive index in the observed wavelength range, the slot-die coating of a colloidal layer increases the refractive index. The increase depends on the size of the colloids, which govern their imbibition properties. Clearly, for small colloids, a mixing layer is observed, which shows a gradual increase of the refractive index from CNF to the colloids at the surface. The large colloids with radii above the average nanopores experience a barrier against imbibition. Thus, the refractive index of this composite material lies between CNF and the small colloid/CNF hybrid. This is readily explained by the filling of the nanopores in the case of slot-die coating of the small colloids. Post-deposition annealing allows for further tuning the refractive index of the hybrid materials. Interestingly, due to the filling of the nanopores, the P(SobMA-co-BMA)$_S$ /CNF hybrid and the PSobMA$_S$ /CNF hybrid thin films do not show a considerable change in refractive index. Thus, the imbibition of the colloids stabilizes the optical properties. Depending on the glass transition temperature, the larger colloid/CNF hybrid, however, shows a different behavior. The P(SobMA-co-BMA)$_L$/CNF hybrid shows a change in refractive index approaching that of the small P(SobMA-co-BMA)$_S$/CNF hybrids. The refractive index of the PSobMA$_L$/CNF hybrid material does not change during the annealing. These nanostructural changes are visualized by AFM, FE-SEM, and GISAXS. AFM and FE-SEM corroborate the tuning of the colloid layer structure by annealing, while GISAXS allows to directly observe the change in colloidal shape (flattening) due to the temperature-induced mobility of the polymer chains. Thus, we are able to directly correlate nanostructure and optical properties in such sustainable, hybrid thin film nanostructures. To conclude, the combination of tailored colloids and annealing offers the possibility to tune the refractive index of the hybrid materials.

5. Experimental Section

Cellulose Nanofibrils: Cellulose nanofibrils with a radius of around 2.5 nm and a length of around 600 nm were produced by 60% Norwegian spruce and 40% Scots pine. The surface of the CNF was negatively charged to due their chemical treatment with 2,2,6,6,-tetramethylpiperidine-1-oxyl (TEMPO)-mediated oxidation reaction, where the free –CH_2OH oxidized to COOH. This treatment gives the CNFs a negative surface charge, in this case, a surface charge of 1000 µmol g^{-1} was used. The gel-like suspension was diluted to a 0.07 wt% and treated by mechanical mixer (12 000 rpm, 10 min, Ultra Turrax, IKA, Germany) and sonication (10 min, BANDELIN SONOPULS HD/UW 2070, Germany). In addition, this solution was centrifuged (5000 rpm, 60 min, Rotina 420, Hettich GmbH & Co. KG, Germany).

Colloids: The basic synthesis and physicochemical properties of the colloids (PSobMA$_S$, PSobMA$_L$, P(SobMA-co-BMA)$_S$, P(SobMA-co-BMA)$_L$) which were deposited on the cellulose surfaces are described in ref. [33]. In short, the colloids were based on sobrerol which is a terpene-derived monomer, and via reversible addition-fragmentation chain transfer polymerization (RAFT) coupled with polymerization-induced self-assembly (PISA) the synthesis of poly(sobrerol methacrylate) (PSobMA) was accomplished. In the case of PSobMA$_S$, conventional emulsion polymerization was used. A second batch of colloids with similar size but lower glass transition temperature T_g was synthesized by homo- and copolymerizing sobrerol methacrylate with butyl methacrylate (BMA) following the same technique. The colloids were stabilized by a hydrophilic shell polymer (protonated poly(dimethylaminoethyl methacrylate) for the cases of PSobMA$_S$ and P(SobMA-co-BMA)$_S$– where RAFT-mediated PISA was used –and by cetyltrimethylammonium chloride (CTAC) for PSobMA$_L$ and P(SobMA-co-BMA)$_L$) for the case of emulsion polymerization, and they were dispersed in water which facilitates the deposition on CNF. The used colloidal ink had a concentration of 0.1 wt% in aqueous dispersion. The resulting colloids had similar sizes to the previous work of the group on wettability tuning of the surface by poly(methyl methacrylate) colloids.[71]

Sample Preparation: The CNF suspension was slot-die coated on a 75 × 25 mm^2 precleaned, polished silicon wafer (Si-Mat, Germany). Cleaning was performed by sonication in acetone and 2-propanol for 15 min each. Subsequently, the wafers were piranha cleaned for 15 min and UV/ozone-plasma-treated for 20 min. The slot-die coating of the CNF layer on the silicon wafer and the colloidal layer on the CNF was performed with a custom-made slot-die coater.[61] The print head was filled with a remotely controlled syringe. To print the CNF layer on the silicon wafer, a pump rate of 0.2 ml s^{-1} and a velocity of 50 mm s^{-1} of the printer head were used. The silicon wafer was heated to 80 °C during printing. Seventy printing cycles were performed to fabricate a blue-colored CNF template. Between the cycles, the slot-die-coated layers were dried in 5 s, before the next printing cycle was initiated. The colloidal layer was applied in one single cycle on top of the CNF layer. The resulting hybrid thin films were named PSobMA$_{L,S}$/CNF and P(SobMA-co-BMA)$_{L,S}$/CNF the subscript indicating the size of the colloids.

Spray Deposition: For reference, a sprayed CNF layer was deposited on a 75 × 25 mm^2 precleaned silicon wafer as above. The spray protocol is described in previous work.[44] The CNF dispersion concentration was the same as the CNF dispersion used for slot-die coating.

Grazing Incidence X-Ray Scattering: GISAXS was performed at the beamline P03 at PETRA III, DESY, Hamburg, using a photon energy of 11.8 keV, a beam size of 30 × 25 µm^2, and an incident angle of $\alpha_i = 0.4°$.[78] The sample detector distance was SDD_{GISAXS} = 3098 mm. The GISAXS detector was a PILATUS 2 M detector (Dectris Ltd., Switzerland) with a pixel size of 172 × 172 µm^2 per pixel. The acquisition time was 0.5 s. The data analysis was done following the procedure described in the work by Schaffer et al.,[46] In short, a real-space model using form and structure factor (i.e., radius and distance with corresponding polydispersity) with local monodisperse approximation was used for describing distorted wave-Born approximation effects in the horizontal cut of the GISAXS pattern. For the annealing experiment, the samples were heated up to the corresponding temperature and held there for 5 min for temperature stabiliza-

© 2023 The Authors. Advanced Optical Materials published by Wiley-VCH GmbH

tion prior to each measurement. The GISAXS measurements for each temperature were conducted in 5 min. During the GISAXS measurement, the sample was scanned laterally through the beam to avoid radiation damage.

Spectroscopic Ellipsometry: Spectroscopic ellipsometry was performed with a J.A. Woollam, M-2000.[79] Fitting of the optical constants was performed with the J.A. Woollam software (CompleteEASE 6.54). The used spectral range was from 201 nm up to 1000 nm. The samples were measured under angles of [45°, 50°, 55°, 60°, 65°, 70°, and 75°] with respect to the sample normal and with a sampling time of 10 s with focus lenses installed. The optical microscope was used to choose the region of interest. Details are shown in Figures S1, S2, S14, and S15 and Table S1, Supporting Information. The fitting and the error calculation were based on the fitting software which was based on Levenberg–Marquardt.

Polarized Optical Microscopy: Polarized optical microscopy was performed using a VHX-7000N (Keyence) with crossed polarizers. Results are shown in Figure S16, Supporting Information.

Atomic Force Microscopy: For the AFM measurements, the Dimension Icon AFM from Bruker was used. The surface topography images were created using tapping mode in air, as tip the model RTESPA-300 (Antimony [n] doped Si with a resonance frequency of 300 kHz) was used. The image resolution was 512 × 512 pixels, and the scan rate was 0.5 Hz.

Field-Emission Scanning Electron Microscopy: FE-SEM images were taken with the high-resolution field emission instrument Nova NanoSEM 450.[80] For the secondary electron images, a through lens detector at an accelerating voltage of 1 kV and a working distance of 1 mm was chosen.

Thickness Measurements: The thickness measurements were performed using a stylus profiler instrument (Dektak, Bruker Corporation, Germany). The tip type was a stylus with a radius of 2 µm and a force of 1 mg.

Supporting Information

Supporting Information is available from the Wiley Online Library or from the author.

Acknowledgements

C.H. acknowledges funding from the DESY innovation fund and Y.B. and S.V.R. acknowledges funding from (DFG, German Research Foundation, RO4638/3-1). A.E.A. and E.M. acknowledge funding from the Knut and Alice Wallenberg Foundation (KAW) through the Wallenberg Wood Science Center. G.P. and H.Z. acknowledge financial support from the Chinese Scholarship Council (CSC) and M.A.R and P.M.-B. from Deutsche Forschungsgemeinschaft (DFG, German Research Foundation) under Germany's Excellence Strategy – EXC 2089/1 – 390776260 (e conversion). The authors acknowledge DESY (Hamburg, Germany), a member of the Helmholtz Association HGF, for the provision of experimental facilities. Parts of this research were carried out at PETRA III and we would like to thank Andrei Chumakov and Jan Rubeck for assistance in using P03. Beamtime was allocated for proposal I-20211570.

Open access funding enabled and organized by Projekt DEAL.

Conflict of Interest

The authors declare no conflict of interest.

Data Availability Statement

The data that support the findings of this study are available from the corresponding author upon reasonable request.

Keywords

cellulose nanofibrils, colloidal films, grazing incidence X-ray and neutron scattering, refractive index, thin films

Received: December 20, 2022
Revised: February 20, 2023
Published online: April 5, 2023

[1] K. Li, C. Li, H. Li, M. Li, Y. Song, *iScience* **2021**, *24*, 102121.
[2] J. Ren, Y. Wang, Y. Yao, Y. Wang, X. Fei, P. Qi, S. Lin, D. L. Kaplan, M. J. Buehler, S. Ling, *Chem. Rev.* **2019**, *119*, 12279.
[3] E. R. Dufresne, H. Noh, V. Saranathan, S. G. J. Mochrie, H. Cao, R. O. Prum, *Soft Matter* **2009**, *5*, 1792.
[4] S. A. S. Mapari, A. S. Meyer, U. Thrane, *J. Agric. Food Chem.* **2009**, *57*, 6253.
[5] R. E. Rodríguez, S. P. Agarwal, S. An, E. Kazyak, D. Das, W. Shang, R. Skye, T. Deng, N. P. Dasgupta, *ACS Appl. Mater. Interfaces* **2018**, *10*, 4614.
[6] M. Rothammer, C. Zollfrank, K. Busch, G. von Freymann, *Adv. Opt. Mater.* **2021**, *9*, 2100787.
[7] J. K. Pi, J. Yang, Q. Zhong, M. B. Wu, H. C. Yang, M. Schwartzkopf, S. V. Roth, P. Müller-Buschbaum, Z. K. Xu, *ACS Appl. Nano Mater.* **2019**, *2*, 4556.
[8] H. Fudouzi, Y. Xia, *Langmuir* **2003**, *19*, 9653.
[9] J. Fontana, J. Naciri, R. Rendell, B. R. Ratna, *Adv. Opt. Mater.* **2013**, *1*, 100.
[10] C. Liu, L. Zhang, X. Zhang, Y. Jia, Y. Di, Z. Gan, *ACS Appl. Mater. Interfaces* **2020**, *12*, 40979.
[11] L. Cai, Y. Wang, L. Sun, J. Guo, Y. Zhao, *Adv. Opt. Mater.* **2021**, *9*, 2100831.
[12] S. F. Liew, J. Yang, H. Noh, C. F. Schreck, E. R. Dufresne, C. S. O'Hern, H. Cao, *Phys. Rev. A* **2011**, *84*, 063818.
[13] S. R. Sellers, W. Man, S. Sahba, M. Florescu, *Nat. Commun.* **2017**, *8*, 14439.
[14] F. Utel, L. Cortese, D. S. Wiersma, L. Pattelli, *Adv. Opt. Mater.* **2019**, *7*, 1900043.
[15] D. Qu, O. J. Rojas, B. Wei, E. Zussman, *Adv. Opt. Mater.* **2022**, *10*, 2201201.
[16] K. W. Klockars, B. L. Tardy, M. Borghei, A. Tripathi, L. G. Greca, O. J. Rojas, *Biomacromolecules* **2018**, *19*, 2931.
[17] A. G. Dumanli, G. Kamita, J. Landman, H. van der Kooij, B. J. Glover, J. J. Baumberg, U. Steiner, S. Vignolini, *Adv. Opt. Mater.* **2014**, *2*, 646.
[18] H. Cong, B. Yu, S. Wang, L. Qi, J. Wang, Y. Ma, *Opt. Express* **2013**, *21*, 17831.
[19] J. D. Forster, H. Noh, S. F. Liew, V. Saranathan, C. F. Schreck, L. Yang, J. C. Park, R. O. Prum, S. G. J. Mochrie, C. S. O'Hern, H. Cao, E. R. Dufresne, *Adv. Mater.* **2010**, *22*, 2939.
[20] S. Chandra, A. Sciortino, S. Shandilya, L. Fang, X. Chen, Nonappa, H. J., L. Johansson, M. Cannas, J. Ruokolainen, R. H. A. Ras, F. Messina, B. Peng, O. Ikkala, *Adv. Opt. Mater.* **2023**, *11*, 2201901.
[21] N. Mittal, R. Jansson, M. Widhe, T. Benselfelt, K. M. O. Håkansson, F. Lundell, M. Hedhammar, L. D. Söderberg, *ACS Nano* **2017**, *11*, 5148.
[22] H. Jung, K. Min, H. Jeon, S. Kim, *Adv. Opt. Mater.* **2016**, *4*, 1738.
[23] K. Copenhaver, K. Li, L. Wang, M. Lamm, X. Zhao, M. Korey, D. Neivandt, B. Dixon, S. Sultana, P. Kelly, W. M. Gramlich, H. Tekinalp, D. J. Gardner, S. MacKay, K. Nawaz, S. Ozcan, *Cellulose* **2022**, *29*, 4835.
[24] L. Geng, N. Mittal, C. Zhan, F. Ansari, P. R. Sharma, X. Peng, B. S. Hsiao, L. D. Söderberg, *Macromolecules* **2018**, *51*, 1498.
[25] C. J. Brett, O. K. Forslund, E. Nocerino, L. P. Kreuzer, T. Widmann, L. Porcar, N. L. Yamada, N. Matsubara, M. Månsson, P. Müller-Buschbaum, L. D. Söderberg, S. V. Roth, *Adv. Electron. Mater.* **2021**, *7*, 2100137.
[26] Q. Wang, A. Tang, Y. Liu, Z. Fang, S. Fu, *Nanomaterials* **2016**, *6*, 164.
[27] Q. Chen, C. J. Brett, A. Chumakov, M. Gensch, M. Schwartzkopf, V. Körstgens, L. D. Söderberg, A. Plech, P. Zhang, P. Müller-Buschbaum, S. V. Roth, *ACS Appl. Nano Mater.* **2021**, *4*, 503.

© 2023 The Authors. Advanced Optical Materials published by Wiley-VCH GmbH

[28] S. Zeng, D. Baillargeat, H.-P. Ho, K.-T. Yong, *Chem. Soc. Rev.* **2014**, *43*, 3426.
[29] J. N. Anker, W. P. Hall, O. Lyandres, N. C. Shah, J. Zhao, R. P. Van Duyne, *Nat. Mater.* **2008**, *7*, 442.
[30] C. J. Brett, W. Ohm, B. Fricke, A. E. Alexakis, T. Laarmann, V. Körstgens, P. Müller-Buschbaum, L. D. Söderberg, S. V. Roth, *ACS Appl. Mater. Interfaces* **2021**, *13*, 27696.
[31] V. Y. Chang, C. Fedele, A. Priimagi, A. Shishido, C. J. Barrett, *Adv. Opt. Mater.* **2019**, *7*, 1900091.
[32] Y. Wang, M. Li, J.-K. Chang, D. Aurelio, W. Li, B. J. Kim, J. H. Kim, M. Liscidini, J. A. Rogers, F. G. Omenetto, *Nat. Commun.* **2021**, *12*, 1651.
[33] A. E. Alexakis, J. Engström, A. Stamm, A. V. Riazanova, C. J. Brett, S. V. Roth, P. Syrén, L. Fogelström, M. S. Reid, E. Malmström, *Green Chem.* **2021**, *23*, 2113.
[34] J. Leng, G. Li, X. Ji, Z. Yuan, Y. Fu, H. Li, M. Qin, H. Moehwald, *J. Mater. Chem. C* **2018**, *6*, 2396.
[35] P. Grey, M. Chapa, M. Alexandre, T. Mateus, E. Fortunato, R. Martins, M. J. Mendes, L. Pereira, *Adv. Opt. Mater.* **2021**, *9*, 2001731.
[36] J. R. G. Navarro, J. Rostami, A. Ahlinder, J. B. Mietner, D. Bernin, B. Saake, U. Edlund, *Biomacromolecules* **2020**, *21*, 1952.
[37] P. Liu, X. Guo, F. Nan, Y. Duan, J. Zhang, *ACS Appl. Mater. Interfaces* **2017**, *9*, 3085.
[38] F. Lyzwa, P. Marsik, V. Roddatis, C. Bernhard, M. Jungbauer, V. Moshnyaga, *J. Phys. D: Appl. Phys.* **2018**, *51*, 125306.
[39] Q. Zhong, C. Chen, L. Mi, J. P. Wang, J. Yang, G. P. Wu, Z. K. Xu, R. Cubitt, P. Müller-Buschbaum, *Langmuir* **2020**, *36*, 742.
[40] N. Hu, C. Chen, E. Metwalli, L. Bießmann, C. Herold, J. Fu, R. Cubitt, Q. Zhong, P. Müller-Buschbaum, *Langmuir* **2021**, *37*, 6819.
[41] X. Zhang, L. P. Kreuzer, D. M. Schwaiger, M. Lu, Z. Mao, R. Cubitt, P. Müller-Buschbaum, Q. Zhong, *Soft Matter* **2021**, *17*, 2603.
[42] Y. Häntsch, G. Shang, A. Petrov, M. Eich, G. A. Schneider, *Adv. Opt. Mater.* **2019**, *7*, 1900428.
[43] H. M. A. Ehmann, O. Werzer, S. Pachmajer, T. Mohan, H. Amenitsch, R. Resel, A. Kornherr, K. Stana-Kleinschek, E. Kontturi, S. Spirk, *ACS Macro Lett.* **2015**, *4*, 713.
[44] C. J. Brett, N. Mittal, W. Ohm, M. Gensch, L. P. Kreuzer, V. Körstgens, M. Månsson, H. Frielinghaus, P. Müller-Buschbaum, L. D. Söderberg, S. V. Roth, *Macromolecules* **2019**, *52*, 4721.
[45] M. W. Heindl, T. Kodalle, N. Fehn, L. K. Reb, S. Liu, C. Harder, M. Abdelsamie, L. Eyre, I. D. Sharp, S. V. Roth, P. Müller-Buschbaum, A. Kartouzian, C. M. Sutter-Fella, F. Deschler, *Adv. Opt. Mater.* **2022**, *10*, 2200204.
[46] C. J. Schaffer, C. M. Palumbiny, M. A. Niedermeier, C. Jendrzejewski, G. Santoro, S. V. Roth, P. Müller-Buschbaum, *Adv. Mater.* **2013**, *25*, 6760.
[47] A. Hexemer, P. Müller-Buschbaum, *IUCrJ* **2015**, *2*, 106.
[48] W. Ohm, A. Rothkirch, P. Pandit, V. Körstgens, P. Müller-Buschbaum, R. Rojas, S. Yu, C. J. Brett, D. L. Söderberg, S. V. Roth, *J. Coat. Technol. Res.* **2018**, *15*, 759.
[49] S. V. Roth, G. Santoro, J. F. H. Risch, S. Yu, M. Schwartzkopf, T. Boese, R. Döhrmann, P. Zhang, B. Besner, P. Bremer, D. Rukser, M. A. Rübhausen, N. J. Terrill, P. A. Staniec, Y. Yao, E. Metwalli, P. Müller-Buschbaum, *ACS Appl. Mater. Interfaces* **2015**, *7*, 12470.
[50] S. V. Roth, G. Herzog, V. Körstgens, A. Buffet, M. Schwartzkopf, J. Perlich, M. M. Abul Kashem, R. Döhrmann, R. Gehrke, A. Rothkirch, K. Stassig, W. Wurth, G. Benecke, C. Li, P. Fratzl, M. Rawolle, P. Müller-Buschbaum, *J. Phys.: Condens. Matter* **2011**, *23*, 254208.
[51] A. Alvarez-Fernandez, B. Reid, M. J. Fornerod, A. Taylor, G. Divitini, S. Guldin, *ACS Appl. Mater. Interfaces* **2020**, *12*, 5195.
[52] V. Körstgens, J. Wiedersich, R. Meier, J. Perlich, S. V. Roth, R. Gehrke, P. Müller-Buschbaum, *Anal. Bioanal. Chem.* **2010**, *396*, 139.
[53] G. Herzog, G. Benecke, A. Buffet, B. Heidmann, J. Perlich, J. F. H. Risch, G. Santoro, M. Schwartzkopf, S. Yu, W. Wurth, S. V. Roth, *Langmuir* **2013**, *29*, 11260.
[54] S. V. Roth, R. Döhrmann, R. Gehrke, R. Röhlsberger, K. Schlage, E. Metwalli, V. Körstgens, M. Burghammer, C. Riekel, C. David, P. Müller-Buschbaum, *J. Appl. Crystallogr.* **2015**, *48*, 1827.
[55] A. Barranco, A. Borras, A. R. Gonzalez-Elipe, A. Palmero, *Prog. Mater. Sci.* **2016**, *76*, 59.
[56] V. Körstgens, R. Meier, M. A. Ruderer, S. Guo, H.-Y. Chiang, J. Perlich, S. V. Roth, R. Gehrke, P. Müller-Buschbaum, *Rev. Sci. Instrum.* **2012**, *83*, 076107.
[57] Y. M. Wang, X. T. Tian, H. Zhang, Z. R. Yang, X. B. Yin, *ACS Appl. Mater. Interfaces* **2018**, *10*, 22445.
[58] Q. Li, Y. Zhang, L. Shi, H. Qiu, S. Zhang, N. Qi, J. Hu, W. Yuan, X. Zhang, K.-Q. Zhang, *ACS Nano* **2018**, *12*, 3095.
[59] A. Falco, M. Petrelli, E. Bezzeccheri, A. Abdelhalim, P. Lugli, *Org. Electron.* **2016**, *39*, 340.
[60] J. Li, J. Dagar, O. Shargaieva, M. A. Flatken, H. Köbler, M. Fenske, C. Schultz, B. Stegemann, J. Just, D. M. Többens, A. Abate, R. Munir, E. Unger, *Adv. Energy Mater.* **2021**, *11*, 2003460.
[61] M. A. Reus, L. K. Reb, A. F. Weinzierl, C. L. Weindl, R. Guo, T. Xiao, M. Schwartzkopf, A. Chumakov, S. V. Roth, P. Müller-Buschbaum, *Adv. Opt. Mater.* **2022**, *10*, 2102722.
[62] W. Chen, H. Tang, N. Li, M. A. Scheel, Y. Xie, D. Li, V. Körstgens, M. Schwartzkopf, S. V. Roth, K. Wang, X. W. Sun, P. Müller-Buschbaum, *Nanoscale Horiz.* **2020**, *5*, 880.
[63] W. Song, J. K. Lee, M. S. Gong, K. Heo, W. J. Chung, B. Y. Lee, *ACS Appl. Mater. Interfaces* **2018**, *10*, 10353.
[64] E. Kontturi, P. Laaksonen, M. B. Linder, Nonappa, A. H. G., O. J. Rojas, O. Ikkala, *Adv. Mater.* **2018**, *30*, 1703779.
[65] M. Karg, T. A. F. König, M. Retsch, C. Stelling, P. M. Reichstein, T. Honold, M. Thelakkat, A. Fery, *Mater. Today* **2015**, *18*, 185.
[66] K. S. Wienhold, V. Körstgens, S. Grott, X. Jiang, M. Schwartzkopf, S. V. Roth, P. Müller-Buschbaum, *Sol. RRL* **2020**, *4*, 2000086.
[67] M. Al-Hussein, E. M. Herzig, M. Schindler, F. Löhrer, C. M. Palumbiny, W. Wang, S. V. Roth, P. Müller-Buschbaum, *Polym. Eng. Sci.* **2016**, *56*, 889.
[68] S. V. Roth, M. Kuhlmann, H. Walter, A. Snigirev, I. Snigireva, B. Lengeler, C. G. Schroer, M. Burghammer, C. Riekel, P. Müller-Buschbaum, *J. Phys.: Condens. Matter* **2009**, *21*, 264012.
[69] G. Renaud, R. Lazzari, F. Leroy, *Surf. Sci. Rep.* **2009**, *64*, 255.
[70] R. Blell, X. Lin, T. Lindström, M. Ankerfors, M. Pauly, O. Felix, G. Decher, *ACS Nano* **2017**, *11*, 84.
[71] J. Engström, C. J. Brett, V. Körstgens, P. Müller-Buschbaum, W. Ohm, E. Malmström, S. V. Roth, *Adv. Funct. Mater.* **2020**, *30*, 1907720.
[72] G. Herzog, M. M. Abul Kashem, G. Benecke, A. Buffet, R. Gehrke, J. Perlich, M. Schwartzkopf, V. Körstgens, R. Meier, M. A. Niedermeier, M. Rawolle, M. A. Ruderer, P. Müller-Buschbaum, W. Wurth, S. V. Roth, *Langmuir* **2012**, *28*, 8230.
[73] S. Gruener, P. Huber, *Transp. Porous Media* **2019**, *126*, 599.
[74] A. Isogai, T. Saito, H. Fukuzumi, *Nanoscale* **2011**, *3*, 71.
[75] J. Engström, A. M. Jimenez, E. Malmström, *Nanoscale* **2020**, *12*, 6462.
[76] M. Schöttle, T. Tran, T. Feller, M. Retsch, *Adv. Mater.* **2021**, *33*, 2101948.
[77] E. K. Oikonomou, K. Golemanov, P.-E. Dufils, J. Wilson, R. Ahuja, L. Heux, J.-F. Berret, *ACS Appl. Polym. Mater.* **2021**, *3*, 3009.
[78] A. Buffet, A. Rothkirch, R. Döhrmann, V. Körstgens, M. M. Abul Kashem, J. Perlich, G. Herzog, M. Schwartzkopf, R. Gehrke, P. Müller-Buschbaum, S. V. Roth, *J. Synchrotron Radiat.* **2012**, *19*, 647.
[79] J. A. Woollam, B. D. Johs, C. M. Herzinger, J. N. Hilfiker, R. A. Synowicki, C. L. Bungay, *Proc. SPIE* **1999**, *10294*, 1029402.
[80] A. Stierle, T. F. Keller, H. Noei, V. Vonk, R. Roehlsberger, *J. Large-Scale Res. Facil. JLSRF* **2016**, *2*, A76.

© 2023 The Authors. Advanced Optical Materials published by Wiley-VCH GmbH